# Dynamic mitigation mechanisms of rime icing with propagating surface acoustic waves

# Dynamic mitigation mechanisms of rime icing with propagating surface acoustic waves

*Deyu Yang,[1,#] Luke Haworth,[2,#] Prashant Agrawal,[2] Ran Tao,[3] Glen McHale,[4] Hamdi Torun,[2] James Martin,[2] Jingting Luo,[3] Xianghui Hou,[1,*] YongQing Fu [2,*]*

[1] Faculty of Engineering, University of Nottingham, Nottingham, NG7 2RD, UK

[2] Faculty of Engineering and Environment, Northumbria University, Newcastle upon Tyne, NE1 8ST, UK

[3] Shenzhen Key Laboratory of Advanced Thin Films and Applications, College of Physics and Optoelectronic Engineering, Shenzhen University, Shenzhen, 518060, China

[4] School of Engineering, University of Edinburgh, Edinburgh, EH9 3JL, UK

KEYWORDS: surface acoustic wave, rime ice, phase change, icing technology.

ABSTRACT: Ice accretion on economically valuable and strategically important surfaces poses significant challenges. Current anti/de-icing techniques often have critical issues regarding their efficiency, convenience, long-term stability, or sustainability. As an emerging ice mitigation strategy, thin-film surface acoustic wave (SAW) has great potentials due to its high energy

efficiency and effective integration onto structural surfaces. However, anti/de-icing processes activated by SAWs involve complex interfacial evolution and phase changes, and it is crucial to understand the nature of dynamic solid-liquid-vapor phase changes and ice nucleation, growth, and melting events under the SAW agitations. In this study, we systematically investigated the accretion and removal of porous rime ice on structural surfaces activated by SAWs. We found that icing and de-icing processes are strongly linked with the dynamically interfacial phase and structure changes of rime ice under SAW activations and the acousto-thermally induced localized heating that facilitate the melting of ice crystals. Subsequently, interactions of SAWs with the formed thin water layer at the ice/structure interface result in significant streaming effects that lead to further damage and melting of ice, liquid pumping, jetting, or nebulization.

## Introduction

Ice accretion on structural surfaces is one of the critical hazards in aerospace, power transmission, offshore platform, and wind turbine sectors [1-4]. Based on the ice's morphology and density, there are two major hazardous ice types: rime ice and glaze (or clear) ice. Compared to that of glaze ice, the formation of rime ice is mainly regarded as an instant surface freezing process of supercooled water droplets, with features such as low liquid water contents (generally smaller than 0.1 $g/m^3$), strong supercooling/low temperatures (generally lower than -10 °C), porous (e.g., loose with a high air-filled porosity) and cluster shapes after freezing[5, 6]. The formation of porous structures is mainly due to the quick freezing of the supercooled droplets without residual liquid water that fills the gaps. In low humidity conditions and at subzero

temperatures, supercooled droplets are easily deposited onto the structural surfaces, and then gradually form a thick layer of rime ice[6, 7].

Commonly applied ice mitigation technologies include both passive approaches (such as the use of icephobic surfaces[8]), and active techniques (such as electro-impulsive/expulsive, resistance heating, hot-air bleeding, ultrasonic methods, and chemical fluids[9-13]). However, their efficiency and sustainability for ice protection have significant limitations. For example, icephobic surfaces often have issues of poor mechanical or long-term durability [8, 14]. The chemical fluids used for the removal of accreted ice could cause severe environmental issues[15, 16]. The electrical heating method often consumes excessive energy for ice prevention or removal. Therefore, innovative ice mitigating techniques with high energy efficiency and environment-friendly features are critically required.

Surface acoustic wave (SAW) technologies have been widely applied in wireless communications, acoustofluidics, sensors, particle/cell concentrating, and micro-heaters[17-21]. Multiple wave modes (including Rayleigh, Lamb, Love, and shear horizontal SAWs) and their hybrid waves can be generated and then propagate along the structural surfaces [22, 23]. Compared to the conventional bulk piezoelectric material-based SAW devices, thin film-based SAWs have the advantage that they can integrate multiple functions into a single structure on different substrates, such as silicon, metals, glass, or polymers [24]. Besides the wide applicability on various substrate materials, SAWs can be generated and then propagate on surfaces with different features, even on flexible and bendable surfaces if using thin-film technology [25]. Furthermore, the direction of propagating SAWs can be designed across the whole solid surfaces [26]. Acoustofluidic phenomena generated using thin-film SAW devices, including liquid mixing,

transportation, jetting, nebulization, droplet generation, and particle/biological cell sorting and manipulations, have recently been reported [27-30].

In the field of ice mitigation, thin film-based SAWs have already been demonstrated to effectively generate both acoustic wave vibration and thermal effect on the device surface, thus offering great potentials for both anti-icing and de-icing with a high efficiency [31, 32]. However, interfacial behaviors, ice removal, and prevention mechanisms for both anti-icing and de-icing of the rime ice under propagating SAWs have never been explored. Compared with conventional acoustofluidic research of sensors or lab-on-a-chips using the thin film SAW devices [24, 27, 33, 34], ice protection and mitigation using thin-film SAWs are more complex, mainly because there is varied phase evolution (from solid, liquid, to vapour, or their mixtures) and dynamic evolution of interfacial microstructures during the processes under the agitation of propagating waves. There is a lack of in-depth investigations on the interfacial responses and phase evolution driven by SAWs during the icing and de-icing processes, which restricts the further exploration of SAW devices for ice mitigation.

This study is focused on the anti-icing and de-icing mechanisms of porous rime ice on a structural surface (aluminum plates), integrated with ZnO-based thin film SAWs. We firstly investigate the fundamental issues about interactions of SAWs with the rime ice and/or liquid/ice mixtures. Then we focus on the experimental studies of anti/de-icing performance for rime ice using thin film SAW devices. Finally, the evolution of ice morphology and phase changes at different humidity levels in icing conditions and different SAW powers are investigated, from which the de-icing and anti-icing mechanisms using thin-film SAWs are verified.

**Anti-icing and de-icing of rime ice with SAWs**

Nanoscale surface wave vibrations (induced by the propagating SAWs from the surface into ice or liquid) and the acoustic thermal heating effect are two main mechanisms for ice protection using SAW devices [31]. They play key roles in the anti/de-icing process by preventing ice accumulation and effectively removing the formed ice [31]. In this section, we address this issue by considering the phase evolution of ice, water, and vapour, and connect them with anti/de-icing mechanisms with SAWs. The hypotheses about the anti/de-icing processes and mechanisms are firstly established and then proved by the designed experiments. The whole process can be considered in three different configurations with the presence of (1) solid and dry porous rime ice; (2) the ice/liquid mixture (i.e., some of the ice are partially melted); (3) liquid water/water vapour stage (changed into liquid, and gradually evaporated). Figure 1 illustrates the conceptional anti/de-icing processes with the presence of rime ice on the SAW device in a humid and frozen environment.

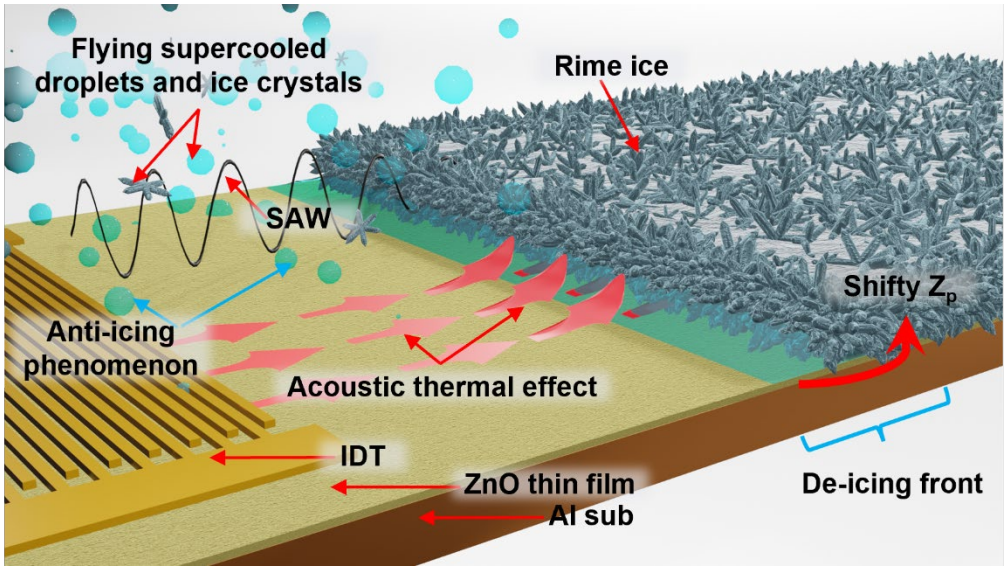


**Figure. 1** Schematic illustration of interfacial behaviors between rime ice and SAW device surface

**SAW induced de-icing process**

***Stage one: solid and porous rime ice***

In the first stage where only solid and porous rime ice crystals exist, the key phenomena at the interface are the propagation of SAWs on the device's surface, mainly through the interface between the device and the porous rime ice. We believe the acoustic impedance of the porous rime ice is a key parameter that affects the propagation of SAWs along the surface of the structure. Currently, there are different theoretical models (such as Biot's theory and Pyett's theory) proposed to investigate the acoustic impedance of snow or rime ice with various densities [35-39]. Most of these models were based on two assumptions, i.e., the acoustic waves have relatively low frequencies (from hundreds to thousands Hz); and the rime ice is a rigid-frame model with a stable structure. However, the structure of real rime ice is highly porous and fragile. To ascertain the transmission of SAW energy from the substrate to the porous rime ice, we use the Johnson-Champoux-Allard (JCA) fluid (such as air) model to determine the acoustic impedance of the porous layer ($Z_p$) [40-44]:

$$Z_p = \sqrt{\rho_{eff} K_{eff}} \tag{1}$$

where,

$$\rho_{eff} = a_\infty \rho_0 \left(1 + \frac{\sigma\phi}{j\omega a_\infty \rho_0} \sqrt{1 + j\omega \frac{4a_\infty^2 \eta \rho_0}{\sigma^2 \Lambda^2 \phi^2}}\right) \tag{2}$$

$$K_{eff} = \gamma_0 P_0 \Bigg/ \left[\gamma_0 - (\gamma_0 - 1)\left(1 + \frac{8\eta}{j\omega P_r \rho_0 \Lambda'^2} \sqrt{1 + j\omega \frac{P_r \rho_0 \Lambda'^2}{16\eta}}\right)^{-1}\right] \tag{3}$$

where $a_\infty$ and $\phi$ are the tortuosity and porosity of the porous layer, $\eta$ and $\rho_0$ are the viscosity and density of the fluid (e.g., air) in the porous layer, $\omega$ is the angular frequency of the wave, $Pr$ is the Prandtl number, σ is the flow resistivity of the porous layer, Λ and $\Lambda'$ are the viscous characteristic length and the thermal characteristic length of the porous layer, $\gamma_0$ is the ratio of specific heats and $P_0$ is the static pressure.

Based on the above background information, Biroun et al. [45] reported that there is a large impedance mismatch between the surface of the SAW devices along with the wave propagation and the porous superhydrophobic nanoparticle layer coating ($\phi \approx 0.57$), which results in a wave reflection coefficient of 0.998, calculated using:

$$R = |(Z_p - Z_{substrate})/(Z_p + Z_{substrate})|^2 \quad (4)$$

This low wave reflection coefficient indicates a weak transmission of acoustic energy at the substrate-porous layer interface. Although it is challenging to quantify the porosity of the rime ice layer, we can reasonably assume that the porosity of the rime ice will be higher than that of the nanoparticle porous coating in Ref. [45]. Therefore, in our case, the SAW acoustic energy will not easily be transmitted through the rime ice layer, thus the energy will be dissipated significantly into the interfacial layer and the rime ice layer. Nanoscale vibrations induced by SAWs easily break the roots of the rime ice clusters, thus changing the structure of porous rime ice and surface ice morphology.

Apart from the significant surface vibrations, the applied radio frequency (RF) power also induces localized heating effect (also called acoustic thermal effect) on the thin film SAW devices due to the SAW energy dissipation. This thermal effect is generated by the high-frequency induced mechanical vibration and stress generated in the substrate [24]. The heating

effect then conducts the viscous dissipation of the acoustic energy into the liquid such as a sessile droplet, as extensively reported in references [20, 46-49].

***Stage two: the solid ice crystals coexist with liquid***

With the activation of SAW energy, the interfacial ice layer is partially melted, thus forming the melted liquid at the interface due to the phase evolution. Once the liquid phase starts to appear at the device/ice interface, the de-icing front at the interface (see Figure 1) will be changed from a porous but rigid rime-ice into an ice-liquid water mixture, which results in a decrease in acoustic impedance. At the interface between water and substrate, if we assumed a reflection coefficient of 0.7 (which is linked with the situation when ice becomes melted), the SAW energy transmitted from the substrate is estimated to increase from 0.2% (with porous rime ice) to 30% (liquid water). Combined with the substrate thermal heating effect, absorption of SAW energy by the melted liquid significantly enhances the exchange of mass and heat inside the liquid due to the internal streaming and liquid flow. The wave-liquid interaction is driven by the SAW streaming force, $F_s$, which is given by [50-52]:

$$F_s = -(1+\vartheta_1^2)^{\frac{2}{3}} A^2 \omega^2 k_i exp2(k_i x + \vartheta_1 k_i y) \quad (5)$$

where $\vartheta_1 = j\vartheta$ (with $j^2 = -1$) is the attenuation constant and $\vartheta^2 = 1 - (v_L/v_S)^2$, and $v_L$ and $v_S$ are the wave velocities in the liquid and on the solid surface, respectively. $A$ is the wave amplitude, $\omega$ is the angular velocity, $k$ is the wave number of the leaky surface acoustic wave, and subscripts $i$ and $j$ =1, 2, 3 represent the $x$, $y$ and $z$ coordinates. Sudeepthi et al. [53] reported the transition of wetting behaviors on a porous and nanoparticulate surface with the application of SAWs. They observed that with the agitation of SAWs, the state of surface droplets was changed

from a Cassie state to a Wenzel state, indicating that SAW agitations caused the surface water to penetrate into the porous layer. Therefore, this indicates that the SAW streaming force can effectively prompt water penetration and propagation into the porous rime ice layer, and also significantly enhance the acoustic thermal effect.

Under the activation of propagating SAWs, this de-icing front quickly moves along the SAW propagating direction, away from the IDT area. With the continued de-icing process, the porous rime ice will shrink gradually until it is changed into multiple independent ice crystals flowing with the internal streaming induced by SAWs. In this case, the semi-melted ice crystals dispersed in the liquid are governed by the acoustic radiation force ($F_R$) and acoustic streaming drag force ($F_d$), which are [54-56]:

$$F_R = -\left(\pi p_0^2 V_p \beta_f \Big/ 2\lambda\right) \varphi(\beta, \rho) \sin\left(4\pi x \Big/ \lambda\right) \tag{6}$$

$$F_d = 6\pi\mu r v \tag{7}$$

where $p_0$ is the acoustic pressure, $V_p$ is the volume of the ice crystals, $\beta$ and $\rho$ are the compressibility and density of the melted liquid and ice crystals, $\varphi$ is the acoustic contrast factor, $\lambda$ is the wavelength of the acoustic waves, $x$ is the distance from the pressure node; $\mu$, $r$, and $v$ are the dynamic viscosity of the liquid, radius and relative velocity of the ice crystals, respectively. The significant flowing of ice crystals can accelerate their elimination and enhance the mass changes inside the liquid.

In brief, after the occurrence of phase changes from solid ice to liquid, the exchange of mass and heat within the rime ice is enhanced by the acoustic pressure and agitations, which effectively promotes the de-icing process.

***Stage three: melted liquid activated by SAWs***

When the ice crystals are completely melted and transformed into a liquid state, the acoustic wave will induce different effects, depending on the applied power. The waves may either drive the liquid away, nebulize the liquid into mists at high power levels, or the generated heat can quickly evaporate the liquid layer from the surface[24].

**Anti-icing mechanisms for rime ice**

Based on the theory of homogeneous ice nucleation in the air, supercooled droplets would be the main phase that flies and is attached to the solid surface, then nucleates, grows and forms the porous rime ice due to the low temperature nucleation centres[6, 57]. However, considering the possible particles in the air (such as dust), some ice crystals may also be initiated in the gas phase from the water vapour. Thus, in this study, both supercooled droplets (the main phase) and ice crystals (the secondary phase) will be discussed in the anti-icing process.

For the newly attached supercooled droplets that are generated in the subzero environment, the SAWs prevent ice nucleation and accretion by restricting the size of ice embryos to be smaller than the critical nucleolus radius, $r_c$, and increasing the critical free energy of heterogeneous ice nucleation, $\Delta G^*$, which has been reported in Ref. [31]. The attached supercooled droplets are also affected by vibration and thermal effects. This hybrid effect offers an advanced platform for acoustofluidics to enhance the impact of both acoustic wave propagation and localized heating

transfer. The attached droplets are easily activated, jetted, or evaporated [24] before the ice nucleation happens, thus significantly preventing or delaying ice formation and accumulation.

When ice crystals are attached to the device surface, similar interfacial reactions which have been discussed in the de-icing process should happen at the interfaces between the ice and the surface. The structures of the surface ice crystals will be broken due to the surface vibrations, while the thermo-heating effect will promote the phase changes and melt the ice into the liquid. The acoustic pressure/forces inside the liquid promote the exchanges of mass and heat which effectively prevent ice formation.

**Method**

***Preparation of SAW device:*** A ZnO film of ~5 μm thick was deposited onto 1.5 mm-thick Al plates using the DC magnetic sputtering technique. A zinc target with 99.99% purity was used during the deposition. The DC power was 400 W and the $Ar/O_2$ gas flow was 10/15 (in the unit of sccm). The crystalline structure of the ZnO film was analyzed using an X-ray diffractometer (XRD, D5000, Siemens) with Ni-filtered Cu-Kα radiation (40 kV, 30 mA, $\lambda = 1.5406$ Å). XRD pattern of the ZnO film on aluminum substrate shows a strong peak of the ZnO (0002) diffraction plane. This indicates the c-axis preferential growth of the Wurtzite structure ZnO film. The interdigital transducers (IDTs) were patterned on top of ZnO thin film using a conventional photolithography and lift-off process. A bilayer of Cr/Au with thicknesses of 20 nm/100 nm was prepared using a thermal evaporator (EDWARDS AUTO306) as the electrode. The IDTs were designed with a wavelength of 400 μm, comprising 30 pairs of electrodes. The corresponding Rayleigh wave frequency measured using the network analyzer was 7.22 MHz.

***Icing and anti-icing process:*** To create a stable and constant icing/anti-icing environment, the experiment was conducted in a freezing chamber that was built based on a cold plate (Para Cooler A, Para Cooler O, Weinkauf Medizintechnik, Germany) with a sealed resin shield. The accurate humidity was achieved using an atomizer (Omron Ultrasonic Nebulizer NE-U17) that generated water aerosols with controlled vaporizing power and imputing speed. The velocity of airflow (~3.8 m/s) and temperature consistency inside the chamber was stabilized using an electric fan. The cold plate was set at -6.5 ℃ which kept the environmental temperature at -1 ℃ and the device temperature at -10 ℃. Before the start of icing, the SAW device was cooled down in the chamber for 20 minutes in advance. Then, the icing process was carried out with RH levels of 60%, 70%, 80%, and 90%, respectively. The anti-icing study was performed with different RH levels and SAW powers (from 0.002 W to 2.300 W). The icing duration was last for 20 minutes while the IDS camera with Navitar 12X objective lens was used to record the ice morphology from the top and side of the device. The mass of rime ice accumulated was measured after the icing process. Each test was repeated 3 times to get the average value. An infrared camera was used to monitor temperature changes of the SAW device surface with the humidity of 25% in the same chamber with the same airflow speed.

***De-icing process:*** To do the de-icing tests, all the samples were cooled down in the chamber with a temperature of -6.5 $^{o}$C for 20 minutes. The de-icing was carried out (for 5 minutes at most) with various RH levels of 60%, 70%, 80%, and 90%, respectively. The SAW reflection signal of $S_{11}$ was measured every 1 minute. After the ice formation, SAW was applied with various powers (from 0.400 W to 2.300 W with proper gaps) to evaluate the de-icing performance. A high-speed camera (HotShot 1280 CC) with Navitar 6.0X zoom lens and 1.5X

objective lens and the IDS camera with Navitar 12X objective lens were also used to record the de-icing process from the top and side view.

## Results and discussions

### Device characterization

The SAW device used in this study was formed on ZnO thin film deposited on a 1.5 mm aluminum plate, and the designed wavelength was 400 μm with a measured Rayleigh resonant frequency of 7.22 MHz. The electromechanical coupling coefficient ($k^2$) of the SAW device is ~1.75%, whereas the temperature coefficient of frequency (TCF) [24] is ~248 ppm/°C (see the supporting information).

The reflection spectra $S_{11}$ of the SAW device (measured at room temperature, sub-zero temperature, and after the icing with various humidity levels at subzone temperature) are shown in Figure S1 in the supporting information. The results show that the ice accretion caused serious damping of SAW signals. All the necessary basic information about the SAW device used in this study is summarized in Table 1.

**Table 1**. Experimental parameters of the SAW device used in this study

| Parameters | Values |
|---|---|
| Materials of piezoelectric thin film | ZnO |
| Materials of substrate | Aluminum sheet with 1.5 mm thickness |
| Wavelength | 400 μm |
| Frequency | 7.22 MHz |
| Electromechanical coupling coefficient ($k^2$) | ~1.75% |
| Temperature coefficient of frequency (TCF) | ~248 ppm/°C |

The thermal heating effect on the surface of the SAW device was characterized using an infrared camera. The obtained temperature changes of the SAW device surface with various SAW powers within 90 seconds in the ambient environment (17 $^{o}$C) and in a cold chamber (-10 $^{o}$C) with 25% humidity are summarized in Figure S2 in the supporting information. Selected infrared images are shown in Figure S3 in the supporting information. As expected, with the increase of applied SAW power, the surface temperature increases. When the SAW power is applied continuously, the recorded temperature changes at a substrate temperature of -10 $^{o}$C become more significant than that of the substrate at room temperature (as shown in Figures S2(a) and 2(b)). The obtained data are summarized in the Supporting information.

**Anti-icing performance under SAWs**

Figures 2(a)-(c) show the icing morphologies formed on the SAW device after 20 minutes, with various applied SAW powers at different RH levels. Figure 2(a) indicates that when there are no SAWs applied, the surface ice layer becomes much thicker with the increase of the RH level as expected. The ice morphology is also changed from a thin ice layer at 60% humidity to the typical ice clusters and thick layer at 90% humidity.

Figure 2(b) shows the icing morphology after a SAW power of 0.002 W was applied under different RH levels. Similar to Figure 2(a), the ice layer becomes much thicker, and the ice crystals grow much larger with the increase of the RH level. However, even at such a low power of 0.002 W, ice accretion is reduced effectively. There is no visible ice in the 60% RH as shown in Figure 2(a). At the other humidity levels, the thickness of the ice layer is much thinner, and the size of ice clusters is smaller as shown in Figure 2(a).

Figure 2(c) shows the icing morphologies in the environment with 90% RH at different SAW powers. Compared to Figure 2(a) without the applied power, the anti-icing effect is significant, even at a low power of 0.060 W, showing only a thinner ice layer and tiny ice crystals. When the power is increased to 0.660 W and 2.300 W, the surface of the device does not show apparent icing phenomena. These results prove that ice accretion can be effectively restrained at low SAW powers.

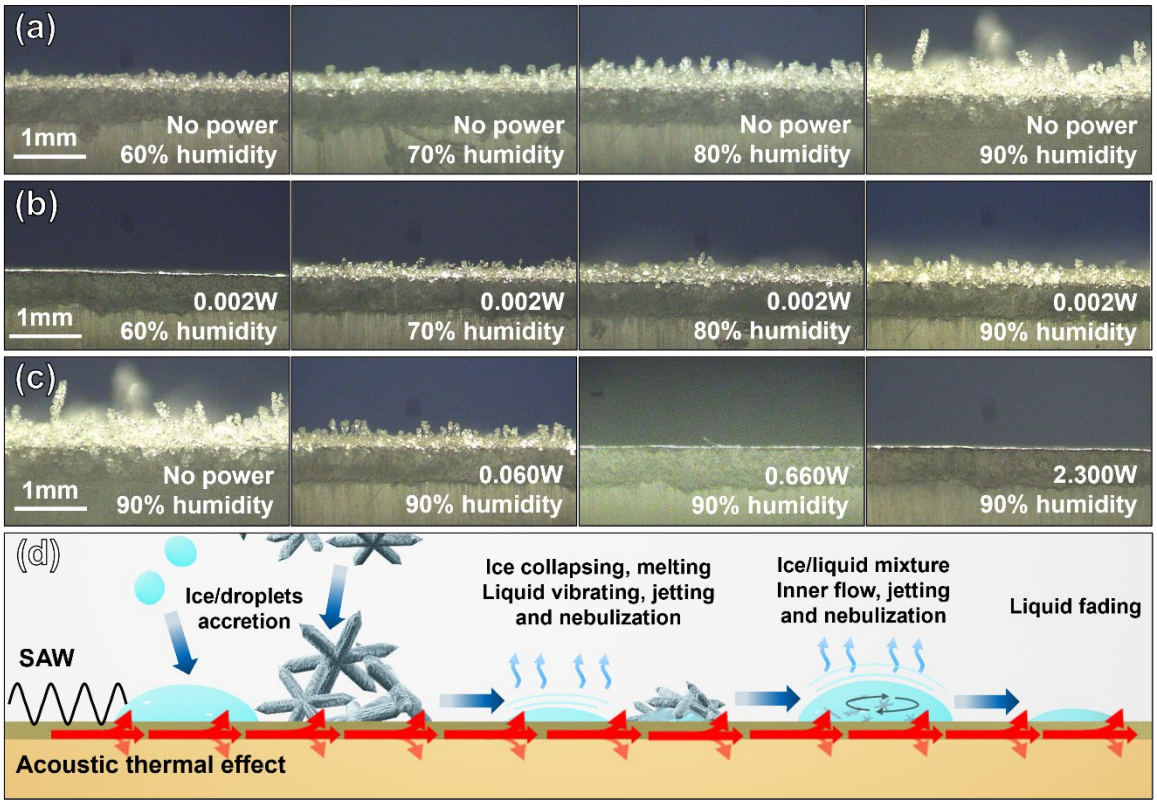


**Figure 2.** Cross-sectional surface or ice morphology after 20-minute icing process: (a) without applying SAW power at different humidity levels; (b) with the power of 0.07 W at different humidity levels; (c) with different SAW powers at 90% humidity; (d) schematic anti-icing process and mechanism on the surface of the SAW device (including the ice/droplets accretion;

ice collapsing and melting; liquid inner flow, vibrating, jetting, nebulization, and then fading gradually).

Figure 3 summarizes the increased mass values of ice accretion on the SAW device without and with various SAW powers at -10 ℃. The mass of ice was calculated by weighing the device before and immediately after the icing process. Generally, the mass of ice is decreased with the increase of SAW power or the decrease of humidity level. When there is no power applied, the ice build-up is around 17.65 mg to 36.50 mg with different humidity levels from 60% to 90%. Once a SAW is applied, even at extremely low powers such as 0.002 W or 0.060 W, the mass of ice is decreased by several milligrams (3.20 mg to 11.80 mg, varied with different RH levels). When the SAW power is increased to 2.300 W, the ice build-up is ranged from around 1.45 mg to 2.10 mg. Combining the results of Figure 2 and Figure 3, it can be found that even at a relatively high power such as 2.30 W, there is always an increase in mass while the surface is dry and clean. The possible reason is that SAWs are generated from the IDT area and propagate along the surface, and they become slightly damped when they propagated far away from the IDT. The images shown in Figure 2 were recorded near the IDT area. The mass increases due to ice formation shown in Figure 3 are the results for the whole surface. Thus, the increase in mass of high powers was caused by the ice/droplet accretion in the area that was away far from the IDTs.

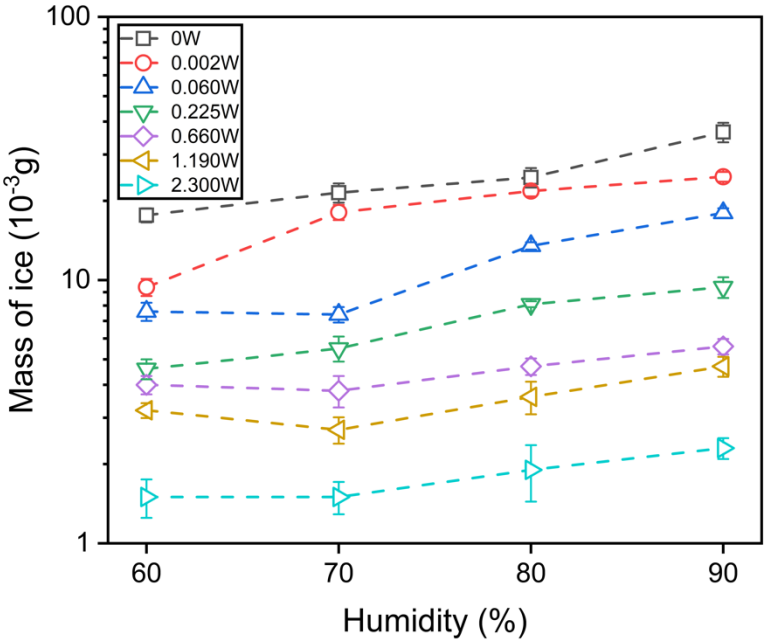


**Figure 3.** Estimated mass values of 20-minute ice accretion on 400 μm wavelength SAW device with various humidity levels and SAW powers.

Based on the above results and discussions in Section 2, a schematic illustration of the anti-icing mechanism under the SAW actuation is illustrated in Figure 2(d). When the arriving supercooled droplets are attached to the surface, the surface acoustic wave induces internal flow by streaming force, while the acoustic thermal effect causes a local heating effect. The ice nucleation is restrained and the exchange of the mass and heating inside the liquid is also enhanced by these two effects, which lead to further ice melting, and liquid pumping, jetting or nebulization, or evaporation, which have been extensively reported in the literature[27, 58, 59]. For the possibly attached ice crystals, the surface vibration induced by the acoustic wave agitates the attached areas of these ice crystals which destroys their structures. At the ice/device interface, the acoustic thermal effect causes a local heating effect, thus the ice crystals are melted easily. The formation of a liquid layer provides a good medium to absorb SAWs, leading to the internal flow

inside the liquid, as explained in Section 2. The further de-icing process is similar to the supercooled droplet route. The experimentally observed phenomena are consistent with those from the hypotheses in Section 2 and prove that the acoustic vibration and localized heating prevent ice nucleation and further accretion.

**De-icing performance under SAWs**

To perform de-icing tests, the rime ice was firstly formed at various RH levels for 20 minutes, and then the SAW power was applied to study the de-icing phenomena. Table 2 lists the obtained de-icing times, which are defined as the durations to remove all the surface rime ice. When the power was low (e.g., 0.400 W), there were no visible changes in the ice morphology at all different RH levels. Similar phenomena were observed when the power was 0.660 W with high RH levels of 70% to 90%. The de-icing was not observed after 5 minutes, and these cases are labeled as N/A as listed in Table 1. Generally, with the increase of SAW power and decrease of the RH level, the de-icing time is decreased systematically. Whereas at certain conditions, results show the opposite trends, e.g., the cases of 0.820 W at 90% humidity and 1.190 W at 60% humidity. A possible reason is that the porous structure of rime ice and the melted liquid lead to the uncontrollable damping of SAW energy, which cannot be prevented during the icing processes.

Based on the obtained results, the specific energy consumption for removing ice can be estimated by:

$$W = {}^{P\tau}/_{m} \tag{8}$$

where $P$ is the SAW power, $\tau$ is the consumed time of removing the ice on the IDT area, $m$ is the mass of ice on the IDT area. Figure 4(a) summarizes the obtained data on energy consumption of the de-icing processes. The general trend observed is that with the increase of input SAW power, energy consumption is much smaller, corresponding to shorter de-icing times. The orange dash line in Figure 4(a) represents the enthalpy of fusion of ice whose value is around 333.55 J/g [60, 61]. As it is well-known, the conventionally used electrothermal de-icing technique generally has low energy efficiency and high energy consumption [12, 62]. Whereas the SAW technology has its advantages such as the high efficiency for the de-icing process because of the combined effects of acoustic vibration and acoustic thermal effects, both of which are localized at the ice/device interface, as reported in Yang *et al.*[31].

**Table 2.** De-icing time (in seconds) with various icing humidity levels and SAW powers

| Humidity | 0.400 W | 0.660 W | 0.820 W | 1.190 W | 2.300 W |
|---|---|---|---|---|---|
| 60% | N/A | 45.8±5 | 7.9±4.1 | 13.1±2.8 | 9.5±0.6 |
| 70% | N/A | N/A | 14.8±1.7 | 17.3±2.5 | 8.4±0.4 |
| 80% | N/A | N/A | 24.0±3.1 | 18.1±1.6 | 7.2±0.8 |
| 90% | N/A | N/A | 16.7±2.0 | 21.0±3.1 | 8.1±0.7 |

Figure 4(b) shows the measured resonant frequency shifts of the SAW devices at different icing stages, which include the results for the surface in a sub-zero environment, iced surface with various RH levels, and de-iced surface with various de-icing powers and RH levels. After the 20-minute icing process, the resonant frequency has been shifted by ~0.1 MHz and the frequency shift becomes much larger with the increase of the RH level. After the de-icing process, the frequency shift is reduced to less than ~0.01 MHz. Meanwhile, if the de-icing power is not high enough, the frequency shift remains a large value at a high humidity level, such as about 0.75 MHz with 0.820 W and 90% humidity.

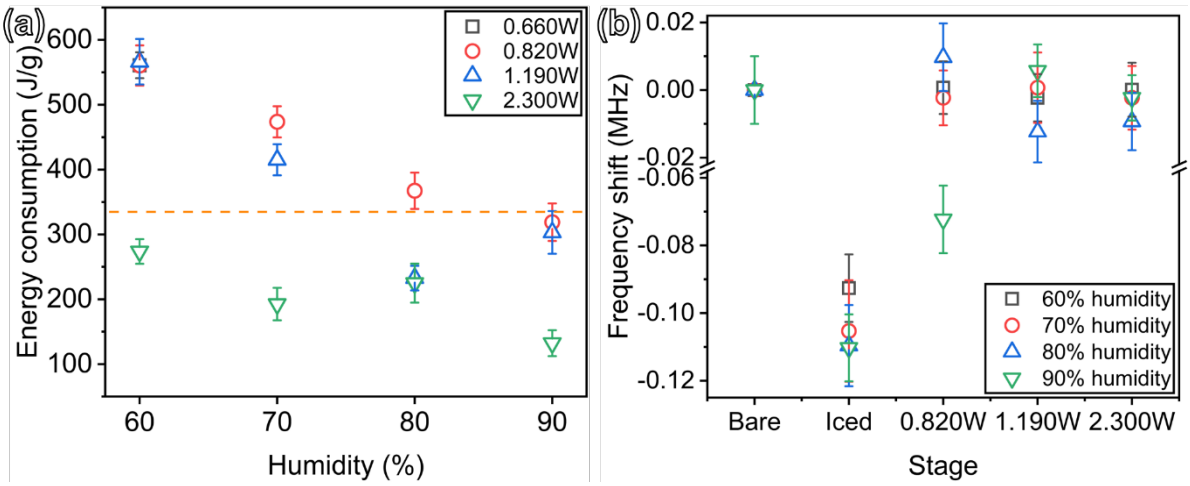


**Figure 4.** (a) Energy consumption of various de-icing processes; (b) resonant frequency shift in different icing and de-icing stages.

Based on the experimental observations, the de-icing process can be summarized in Figures 5(a) to 5(c). There are three major stages during the de-icing process, that match well with those hypotheses explained in Section 2.

The first stage in Figure 5(a) shows that there are no significant visible changes in the ice morphology after the application of SAW powers. However, high-speed images (Figure 5(a)) clearly show that there are dramatic changes in ice clusters or single crystals, which are linked with a local collapse of ice clusters or fracture of the ice crystal structures caused by acoustic wave vibrations. At this initial stage, no apparent phase change (or melting) takes place.

The second stage in Figure 5(b) shows that the phase changes occur and the de-icing front appears. This de-icing front initially starts from the top position of the IDTs. At this stage, the acoustic vibration and thermal heating provide enough energy to the ice crystals to locally melt them into a liquid layer, which is then merged with the ice clusters. These large ice clusters are often seen to collapse into a thin liquid layer. Once the liquid phase appears, the acoustic

streaming force (explained in Equation 5) will drive the liquid into the porous ice layer. With the enhanced exchange of mass and heat induced by the acoustic streaming force, this liquid/ice crystal de-icing front is seen to gradually move along the direction of SAW's propagation. At this stage, most of the ice clusters are remained in their initial states, whereas some of them gradually collapse with the gradual moving of the de-icing front. At this step, ice clusters or crystals still occupy most of the de-icing front, which can be defined as the ice-rich front. While behind this ice-rich front, the liquid layer was quickly evaporated due to the SAW agitation.

With the further de-icing process, the third stage is formed as shown in Figure 5(c). This stage occurs in zones that are often far away from the IDT area. At this stage, the de-icing front becomes much wider. The ice crystals shrink significantly without clear ice cluster morphologies. These semi-melted ice crystals are dispersed in the liquid and driven by acoustic radiation force (Equation 6) and the acoustic streaming drag force (Equation 7) based on the size ranges. The melting becomes significant, and the liquid layer becomes more apparent, which can form a liquid-like front in front of the remaining rime ice. This liquid layer absorbs SAW energy and causes a serious damping effect of the SAW signals. Meanwhile, the acoustic streaming inside the liquid enhances the heat transfer, and also causes significant pumping, jetting, or nebulization effects [24], which we have observed using the high speed camera. These two effects lead to the faster conduction of thermal effect than acoustic waves in the area away from the IDT region. The mixed front with ice and water has been quickly moved along the surface until all the ice disappeared, with the remaining liquid vibrating, nebulizing, or evaporating on the device's surface (see the videos about the de-icing process in the supporting information).

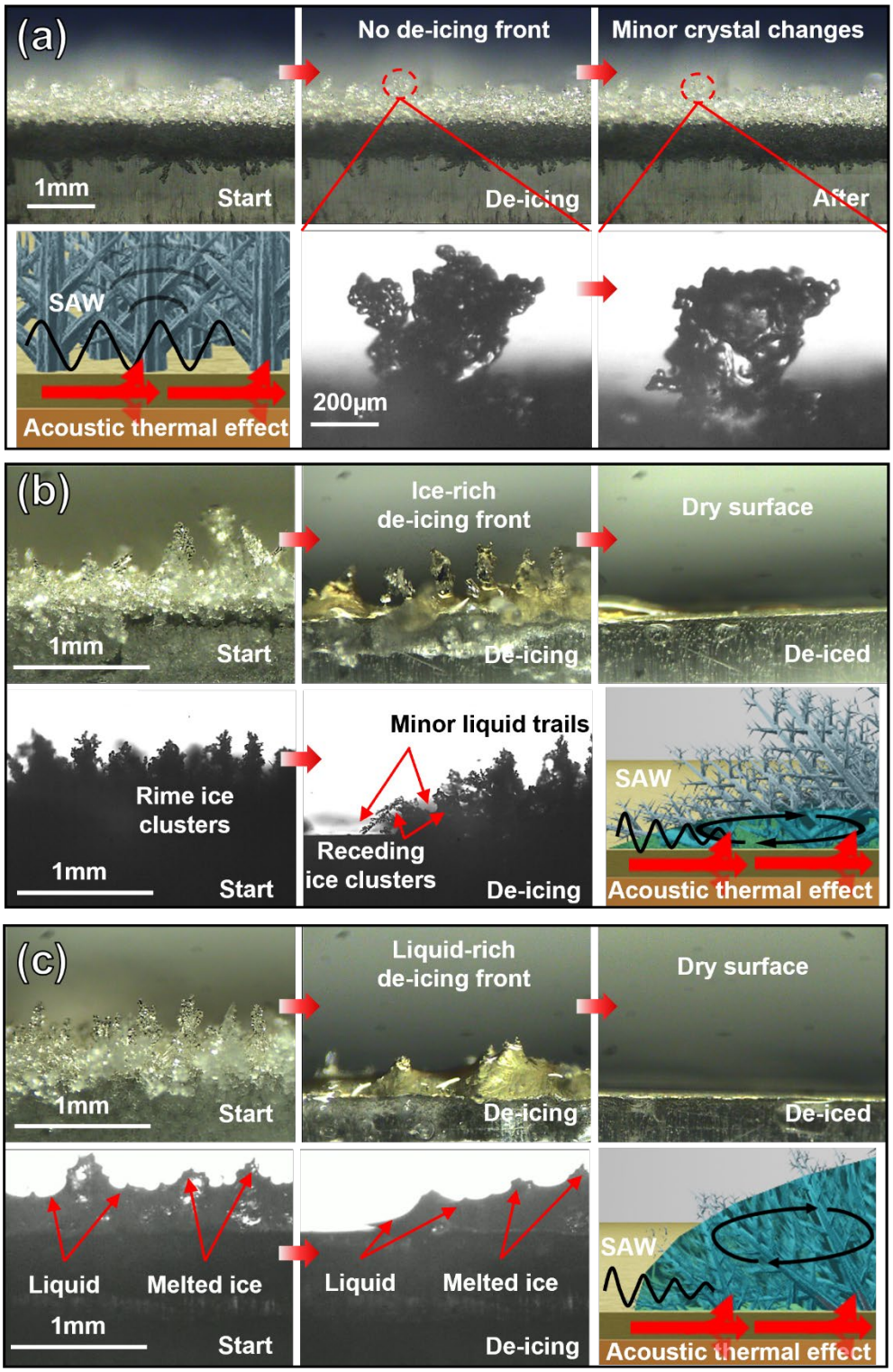


**Figure 5**. (a) the changes of ice morphology or ice crystals before the occurrence of possible phase changes with the propagation of SAW; (b) the de-icing phenomenon of the ice-rich de-

icing front; (c) the de-icing phenomenon of the liquid-rich de-icing front. (The colourful photos were captured by an IDS camera with Navitar 12X objective lens, while the black-and-white photos were captured by a high-speed camera (HotShot 1280 CC) with Navitar 6.0X zoom lens and 1.5X objective lens. The possible illustration of the propagation of SAW at the interfaces was also drawn for different de-icing phenomena.)

Figures 6(a)-(c) show the enlarged de-icing fronts on the SAW device in three stages of the de-icing process. Before the phase changes occur, due to the large differences in acoustic impedance of the porous ice layer with the substrate, the acoustic energy of SAWs is significantly dissipated but confined into the rime ice. This causes significant vibrations of the porous structure, thus leading to plenty of local changes in porous rime ice and its surface crystals.

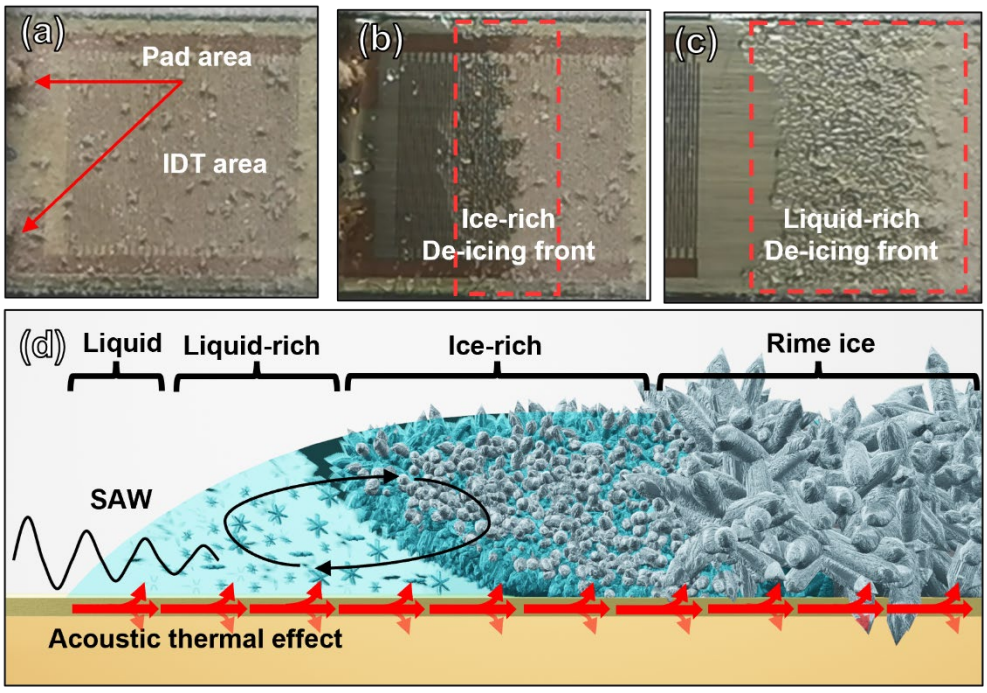

**Figure 6**. (a) Surface morphology of the iced SAW device (in the IDT area, top view); (b) The area with an ice-rich de-icing front; (c) Thea area with a liquid-rich de-icing front; (d) A schematic illustration of the de-icing front with four regions.

With further SAW agitation, phase changes happen, starting near the top area around the IDT. An icing front consisting of liquid/ice mixture is formed and quickly moves along the SAW direction under the hybrid action of the acoustic wave and thermal heating effects. The width of the de-icing front is enlarged obviously with the continuation of the de-icing process (from Figure 6(b) to Figure 6(c)). The de-icing front can be classified into four areas that are the liquid area, the liquid-rich (with ice) area, ice-rich (with liquid) area, and the rime ice area, as shown in Figure 6(d). In the liquid and liquid-rich areas, the SAW wave energy is efficiently absorbed due to low acoustic impedance, thus leading to significant internal streaming and phenomena of liquid transportation, jetting, or nebulization. Some small ice crystals can be seen flowing inside the liquid, stimulated by the acoustic radiation force and the acoustic streaming drag force. In the liquid-rich and ice-rich areas, acoustic wave energy is quickly dissipated into the liquid causing both local heating and significant streaming effects. The acoustic streaming enhances the exchange of mass and heat, which accelerates the de-icing process. In the rime ice area, several events occur including the breakup and collapse of ice crystals or clusters, in the interfacial region between the substrate and rime ice.

In brief, we have confirmed that the key de-icing mechanisms are the phase changes induced by the hybrid effect of acoustic waves and the thermal effect. The surface vibrations induced by the acoustic waves affect the interfacial structures between the rime ice and the device, leading to the break-up and collapse of ice crystals or clusters. With the accumulation of thermal effect, phase change also occurs at the ice/device interface, and the melted liquid and the ice crystals are

quickly merged. Apart from the above two major effects, when the SAW waves propagate into this ice-liquid mixture front, the inner flow and streaming force significantly enhance the exchange of mass and heat which effectively promotes the de-icing process.

## Conclusion

In this study, anti-/de-icing mechanisms of rime ice using thin-film SAW technology were studied systematically. Anti-icing results showed that the anti-icing performance was improved significantly with the increase of the SAW power, and de-icing results showed the de-icing energy efficiency was quite high for the SAW device, even in a severely frozen environment at a high humidity level. By comparing with the potential thermal energy consumption of thermal melting ice, both acoustic wave vibration and acoustic heating play key roles during the de-icing process. The surface vibration induced the breakup and collapse of ice crystals or clusters. The accumulation of heat prompted the melted liquid that absorbed the SAW waves and led to the internal streaming to enhance the exchange of mass and heat. These effects generated further ice melting, liquid pumping, jetting or nebulization, and evaporation during the icing process, while the formation and movement of the de-icing front in the de-icing process were enhanced accordingly.

AUTHOR INFORMATION

**Corresponding Author**

*Dr. Xianghui Hou, email: xianghui.hou@nottingham.ac.uk

*Prof. Richard Fu, email: richard.fu@northumbria.ac.uk.

**Author Contributions**

#: these two authors have the same contribution to this paper.

Y.Q. Fu and X.H. Hou conceived the idea. D.Y. Yang, L. Haworth, X.H. Hou and Y.Q. Fu designed and performed the experimental work. D.Y. Yang and L. Haworth wrote the manuscript and performed analysis. Y.Q. Fu, X.H. Hou, L. Haworth, P. Agrawal, H. Torun, G. McHale, J. Martin, R. Tao, J.T. Luo were involved in the writing, discussion and modification of the article.

**Supporting Information**

Supporting information and video S1 to video S5 are available online.

**Funding Sources**

This work was supported by the Engineering and Physical Sciences Research Council of UK (EPSRC EP/P018998/1), UK Fluids Network Special Interest Group of Acoustofluidics (EP/N032861/1), and EPSRC NetworkPlus in Digitalised Surface Manufacturing (EP/S036180/1).

**Notes**

COMPETING INTERESTS

The authors declare that they have no competing interests.

ABBREVIATIONS

SAW: surface acoustic wave; RH: relative humidity; TCF: temperature coefficient of frequency; IDT: interdigital transducers.

REFERENCES

1. Kudzys, A., Safety of power transmission line structures under wind and ice storms. *Eng. Struct.* **2006,** *28* (5), 682-689.

2. Fortin, G.; Perron, J. In *Wind turbine icing and de-icing*, 47th AIAA Aerospace Sciences Meeting including The New Horizons Forum and Aerospace Exposition, 2009; p 274.

3. Ryerson, C. C., Ice protection of offshore platforms. *Cold Reg Sci Technol* **2011,** *65* (1), 97-110.

4. Zi, G.; Lee, S.-J.; Jang, S. Y.; Yang, S. C.; Kim, S.-S., Investigation of a concrete railway sleeper failed by ice expansion. *Eng. Fail. Anal.* **2012,** *26*, 151-163.

5. Politovich, M. K., Predicting glaze or rime ice growth on airfoils. *J AIRCRAFT* **2000,** *37* (1), 117-121.

6. Pruppacher, H. R.; Klett, J. D., *Microphysics of Clouds and Precipitation*. 2nd ed.; Kluwer Academic Publishers: Boston, 1997.

7. Macklin, W., The density and structure of ice formed by accretion. *Q J ROY METEOR SOC* **1962,** *88* (375), 30-50.

8. Shen, Y.; Wu, X.; Tao, J.; Zhu, C.; Lai, Y.; Chen, Z., Icephobic materials: Fundamentals, performance evaluation, and applications. *Prog Mater Sci* **2019,** *103*, 509-557.

9. Rashid, T.; Khawaja, H. A.; Edvardsen, K., Review of marine icing and anti-/de-icing systems. *J MAR ENG TECHNOL* **2016,** *15* (2), 79-87.

10. Wei, K.; Yang, Y.; Zuo, H.; Zhong, D., A review on ice detection technology and ice elimination technology for wind turbine. *Wind Energy* **2020,** *23* (3), 433-457.

11. Brazil, H.; Conachey, B.; Savage, G.; Baen, P. In *Electrical heat tracing for surface heating on arctic vessels & structures to prevent snow & ice accumulation*, 2012 Petroleum and Chemical Industry Conference (PCIC), IEEE: 2012; pp 1-8.

12. Morita, K.; Kimura, S.; Sakaue, H., Hybrid System Combining Ice-Phobic Coating and Electrothermal Heating for Wing Ice Protection. *Aerospace* **2020,** *7* (8), 102.

13. Wang, Z., Recent progress on ultrasonic de-icing technique used for wind power generation, high-voltage transmission line and aircraft. *Energy Build.* **2017,** *140*, 42-49.

14. Wang, F.; Zhuo, Y.; He, Z.; Xiao, S.; He, J.; Zhang, Z., Dynamic Anti‐Icing Surfaces (DAIS). *Adv. Sci.* **2021,** *8* (21), 2101163.

15. Fay, L.; Shi, X., Environmental impacts of chemicals for snow and ice control: state of the knowledge. *WAT. AIR AND SOIL POLL.* **2012,** *223* (5), 2751-2770.

16. Donadei, V.; Koivuluoto, H.; Sarlin, E.; Vuoristo, P., Durability of Lubricated Icephobic Coatings under Various Environmental Stresses. *Polymers* **2022,** *14* (2), 303.

17. Pan, Y.; Mu, N.; Liu, B.; Cao, B.; Wang, W.; Yang, L., A novel surface acoustic wave sensor array based on wireless communication network. *SENSORS-BASEL* **2018,** *18* (9), 2977.

18. Aubert, T.; Elmazria, O.; Assouar, M. In *Wireless and batteryless surface acoustic wave sensors for high temperature environments*, 2009 9th International Conference on Electronic Measurement & Instruments, IEEE: 2009; pp 2-890-2-898.

19. Gedge, M.; Hill, M., Acoustofluidics 17: Theory and applications of surface acoustic wave devices for particle manipulation. *Lab Chip* **2012,** *12* (17), 2998-3007.

20. Shilton, R. J.; Mattoli, V.; Travagliati, M.; Agostini, M.; Desii, A.; Beltram, F.; Cecchini, M., Rapid and controllable digital microfluidic heating by surface acoustic waves. *Adv Func Mater* **2015,** *25* (37), 5895-5901.

21. Roux-Marchand, T.; Beyssen, D.; Sarry, F.; Elmazria, O., Rayleigh surface acoustic wave as an efficient heating system for biological reactions: Investigation of microdroplet temperature uniformity. *IEEE Trans Ultrason Ferroelectr Freq Control* **2015,** *62* (4), 729-735.

22. Wang, Y.; Xu, Y.; Huang, Q., Progress on ultrasonic guided waves de-icing techniques in improving aviation energy efficiency. *Renew Sust Energ Rev* **2017,** *79*, 638-645.

23. Daniliuk, V.; Xu, Y.; Liu, R.; He, T.; Wang, X., Ultrasonic de-icing of wind turbine blades: Performance comparison of perspective transducers. *Renew Energy* **2020,** *145*, 2005-2018.

24. Fu, Y. Q.; Luo, J.; Nguyen, N.-T.; Walton, A.; Flewitt, A. J.; Zu, X.-T.; Li, Y.; McHale, G.; Matthews, A.; Iborra, E., Advances in piezoelectric thin films for acoustic biosensors, acoustofluidics and lab-on-chip applications. *Prog Mater Sci* **2017,** *89*, 31-91.

25. Tao, R.; Wang, W.; Luo, J.; Hasan, S. A.; Torun, H.; Canyelles-Pericas, P.; Zhou, J.; Xuan, W.; Cooke, M.; Gibson, D., Thin film flexible/bendable acoustic wave devices: Evolution, hybridization and decoupling of multiple acoustic wave modes. *Surf. Coat. Technol.* **2019,** *357*, 587-594.

26. Wang, Y.; Zhang, Q.; Tao, R.; Xie, J.; Canyelles-Pericas, P.; Torun, H.; Reboud, J.; McHale, G.; Dodd, L. E.; Yang, X.; Luo, J.; Wu, Q.; Fu, Y. Q., Flexible/bendable acoustofluidics based on thin-film surface acoustic waves on thin aluminum sheets. *ACS Appl. Mater. Interfaces.* **2021,** *13* (14), 16978-16986.

27. Du, X.; Fu, Y. Q.; Luo, J.; Flewitt, A.; Milne, W., Microfluidic pumps employing surface acoustic waves generated in ZnO thin films. *J. Appl. Phys.* **2009,** *105* (2), 024508.

28. Luong, T.-D.; Phan, V.-N.; Nguyen, N.-T., High-throughput micromixers based on acoustic streaming induced by surface acoustic wave. *Microfluid. Nanofluid.* **2011,** *10* (3), 619-625.

29. H. Biroun, M.; Rahmati, M.; Tao, R.; Torun, H.; Jangi, M.; Fu, Y., Dynamic behavior of droplet impact on inclined surfaces with acoustic waves. *Langmuir* **2020,** *36* (34), 10175-10186.

30. Wang, Z.; Zhe, J., Recent advances in particle and droplet manipulation for lab-on-a-chip devices based on surface acoustic waves. *Lab Chip* **2011,** *11* (7), 1280-1285.

31. Yang, D.; Tao, R.; Hou, X.; Torun, H.; McHale, G.; Martin, J.; Fu, Y., Nanoscale "Earthquake" Effect Induced by Thin Film Surface Acoustic Waves as a New Strategy for Ice Protection. *Adv. Mater. Interfaces* **2021,** *8* (2), 2001776.

32. Zeng, X.; Yan, Z.; Lu, Y.; Fu, Y.; Lv, X.; Yuan, W.; He, Y., Reduction of Ice Adhesion Using Surface Acoustic Waves: Nanoscale Vibration and Interface Heating Effects. *Langmuir* **2021,** *37* (40), 11851-11858.

33. Fu, Y.-Q.; Pang, H.-F.; Torun, H.; Tao, R.; McHale, G.; Reboud, J.; Tao, K.; Zhou, J.; Luo, J.; Gibson, D.; Luo, J.; Hu, P., Engineering inclined orientations of piezoelectric films for integrated acoustofluidics and lab-on-a-chip operated in liquid environments. *Lab Chip* **2021,** *21* (2), 254-271.

34. Fu, Y. Q.; Luo, J.; Du, X.; Flewitt, A.; Li, Y.; Markx, G.; Walton, A.; Milne, W., Recent developments on ZnO films for acoustic wave based bio-sensing and microfluidic applications: a review. *SENSOR ACTUAT B-CHEM* **2010,** *143* (2), 606-619.

35. Buser, O., A rigid frame model of porous media for the acoustic impedance of snow. *J. Sound Vib.* **1986,** *111* (1), 71-92.

36. ISHIDA, T., Acoustic properties of snow. *Contributions from the Institute of Low Temperature Science* **1965,** *20*, 23-63.

37. Marco, O.; Buser, O.; Villemain, P.; Touvier, F.; Revol, P., Acoustic impedance measurement of snow density. *Ann. Glaciol.* **1998,** *26*, 92-96.

38. Iwase, T.; Sakuma, T.; Yoshihisa, K. In *Measurements on sound propagation characteristics in snow layer*, 17th International Congress on Acoustics, Roma, Italy, 2001.

39. Nicolas, J.; Berry, J. L.; Daigle, G., Propagation of sound above a finite layer of snow. *J. Acoust. Soc. Am.* **1985,** *77* (1), 67-73.

40. Liu, Z.; Zhan, J.; Fard, M.; Davy, J. L., Acoustic properties of multilayer sound absorbers with a 3D printed micro-perforated panel. *APPL ACOUST* **2017,** *121*, 25-32.

41. Kinsler, L. E.; Frey, A. R.; Coppens, A. B.; Sanders, J. V., *Fundamentals of acoustics*. John wiley & sons: 2000.

42. Du Plessis, J. P.; Masliyah, J. H., Flow through isotropic granular porous media. *Transp. Porous Media* **1991,** *6* (3), 207-221.

43. Johnson, D. L.; Koplik, J.; Dashen, R., Theory of dynamic permeability and tortuosity in fluid-saturated porous media. *J. Fluid Mech.* **1987,** *176*, 379-402.

44. Liu, Z.; Fard, M.; Jazar, R. *Development of an acoustic material database for vehicle interior trims*; 0148-7191; SAE Technical Paper: 2015.

45. Biroun, M. H.; Haworth, L.; Agrawal, P.; Orme, B.; McHale, G.; Torun, H.; Rahmati, M.; Fu, Y., Surface Acoustic Waves to Control Droplet Impact onto Superhydrophobic and Slippery Liquid-Infused Porous Surfaces. *ACS Appl. Mater. Interfaces.* **2021,** *13* (38), 46076-46087.

46. Kondoh, J.; Shimizu, N.; Matsui, Y.; Sugimoto, M.; Shiokawa, S., Development of temperature-control system for liquid droplet using surface acoustic wave devices. *SENSOR ACTUAT A-PHYS* **2009,** *149* (2), 292-297.

47. Huang, Q.-Y.; Sun, Q.; Hu, H.; Han, J.-L.; Lei, Y.-L., Thermal effect in the process of surface acoustic wave atomization. *Exp. Therm Fluid Sci.* **2021,** *120*, 110257.

48. Mehmood, M.; Chaudhary, T. N.; Burnside, S.; Khan, U. F.; Fu, R. Y.; Chen, B., Coupling mechanism of kinetic and thermal impacts of Rayleigh surface acoustic waves on the microdroplet. *Exp. Therm Fluid Sci.* **2021**, 110580.

49. Wang, Y.; Zhang, Q.; Tao, R.; Chen, D.; Xie, J.; Torun, H.; Dodd, L. E.; Luo, J.; Fu, C.; Vernon, J.; Canyelles-Pericas, P.; Binns, R.; Fu, Y., A rapid and controllable acoustothermal microheater using thin film surface acoustic waves. *SENSOR ACTUAT A-PHYS* **2021,** *318*, 112508.

50. Bruckenstein, S.; Shay, M., Experimental aspects of use of the quartz crystal microbalance in solution. *Electrochim. Acta* **1985,** *30* (10), 1295-1300.

51. Shiokawa, S.; Matsui, Y.; Ueda, T., Study on SAW streaming and its application to fluid devices. *Jpn. J. Appl. Phys.* **1990,** *29* (S1), 137.

52. Tao, R.; McHale, G.; Reboud, J.; Cooper, J. M.; Torun, H.; Luo, J.; Luo, J.; Yang, X.; Zhou, J.; Canyelles-Pericas, P., Hierarchical nanotexturing enables acoustofluidics on slippery yet sticky, flexible surfaces. *Nano Lett.* **2020,** *20* (5), 3263-3270.

53. Sudeepthi, A.; Yeo, L.; Sen, A., Cassie‐Wenzel wetting transition on nanostructured superhydrophobic surfaces induced by surface acoustic waves. *Appl Phys Lett* **2020,** *116* (9), 093704.

54. Yosioka, K.; Kawasima, Y., Acoustic radiation pressure on a compressible sphere. *Acta Acust. united Acust.* **1955,** *5* (3), 167-173.

55. Muller, P. B.; Barnkob, R.; Jensen, M. J. H.; Bruus, H., A numerical study of microparticle acoustophoresis driven by acoustic radiation forces and streaming-induced drag forces. *Lab Chip* **2012,** *12* (22), 4617-4627.

56. Wu, M.; Ozcelik, A.; Rufo, J.; Wang, Z.; Fang, R.; Huang, T. J., Acoustofluidic separation of cells and particles. *Microsyst. Nanoeng.* **2019,** *5* (1), 1-18.

57. Libbrecht, K. G., The physics of snow crystals. *Rep. Prog. Phys.* **2005,** *68* (4), 855.

58. Li, J.; Biroun, S. H.; Tao, R.; Wang, Y.; Torun, H.; Xu, N.; Rahmati, M.; Li, Y.; Gibson, D.; Fu, C.; Luo, J. T.; Dong, L.; Xie, J.; Fu, Y. Q., Wide range of droplet jetting angles by thin-film based surface acoustic waves. *J PHYS D APPL PHYS* **2020,** *53*, 355402.

59. Guo, Y.; Dennison, A.; Li, Y.; Luo, J.; Zu, X.-T.; Mackay, C.; Langridge-Smith, P.; Walton, A.; Fu, Y. Q., Nebulization of water/glycerol droplets generated by ZnO/Si surface acoustic wave devices. *Microfluid. Nanofluid.* **2015,** *19* (2), 273-282.

60. Ott, J. B.; Boerio-Goates, J., *Chemical Thermodynamics: Advanced Applications: Advanced Applications*. Elsevier: 2000.

61. Jones, L.; Atkins, P. W., *Chemical principles: the quest for insight*. Freeman: 1999.

62. Fakorede, O.; Feger, Z.; Ibrahim, H.; Ilinca, A.; Perron, J.; Masson, C., Ice protection systems for wind turbines in cold climate: characteristics, comparisons and analysis. *Renew Sust Energ Rev* **2016,** *65*, 662-675.

ToC Figure

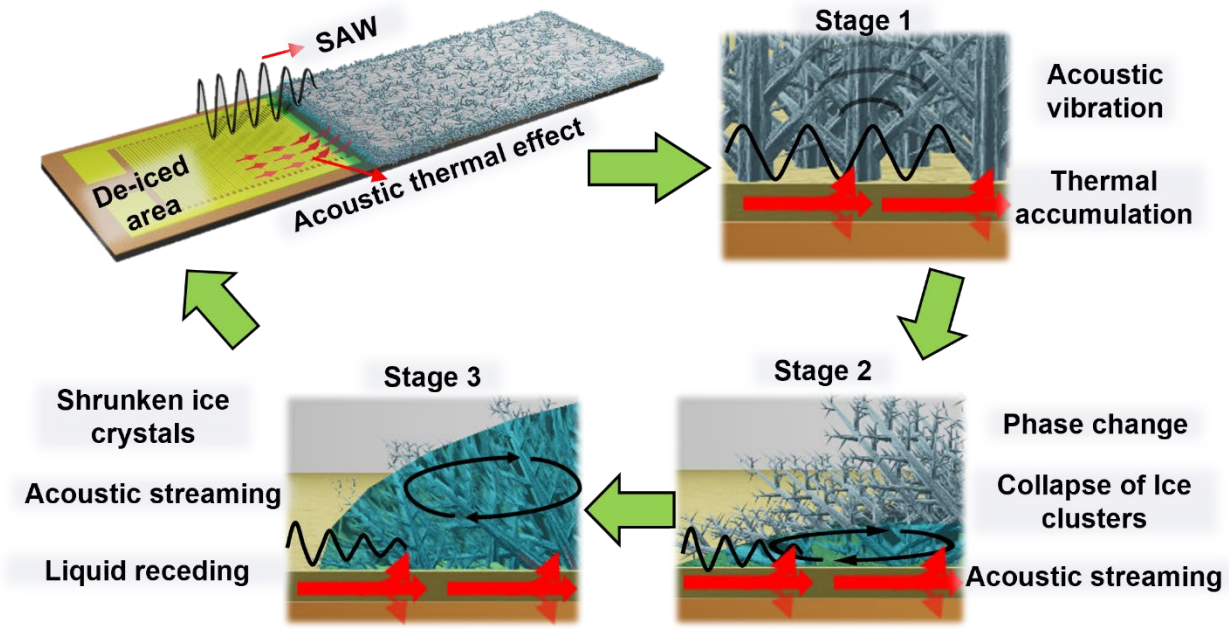
SAW
De-iced area
Acoustic thermal effect
Stage 1
Acoustic vibration
Thermal accumulation
Stage 2
Phase change
Collapse of Ice clusters
Acoustic streaming
Stage 3
Shrunken ice crystals
Acoustic streaming
Liquid receding